

Hyperspectral Luminescence Imaging in Combination with Signal Deconvolution Enables Reliable Multi-Indicator-Based Chemical Sensing

Silvia E. Zieger,* Maria Mosshammer, Michael Kühn, and Klaus Koren*



Cite This: <https://dx.doi.org/10.1021/acssensors.0c02084>



Read Online

ACCESS |



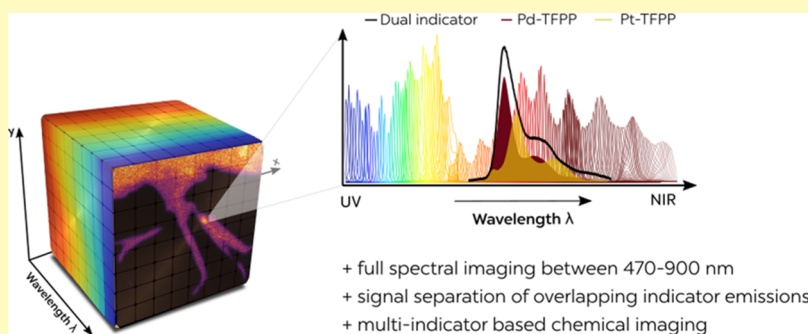
Metrics & More



Article Recommendations



Supporting Information



ABSTRACT: Although real-time monitoring of individual analytes using reversible optical chemical sensors (optodes) is well established, it remains a challenge in optical sensing to monitor multiple analyte concentrations simultaneously. Here, we present a novel sensing approach using hyperspectral imaging in combination with signal deconvolution of overlapping emission spectra of multiple luminescent indicator dyes, which facilitates multi-indicator-based chemical imaging. The deconvolution algorithm uses a linear combination model to describe the superimposed sensor signals and employs a sequential least-squares fit to determine the percent contribution of the individual indicator dyes to the total measured signal. As a proof of concept, we used the algorithm to analyze the measured response of an O_2 sensor composed of red-emitting Pd(II)/Pt(II) porphyrins and NIR-emitting Pd(II)/Pt(II) benzoporphyrins with different sensitivities. This facilitated chemical imaging of O_2 over a wide dynamic range (0–950 hPa) with a hyperspectral camera system (470–900 nm). The applicability of the novel method was demonstrated by imaging the O_2 distribution in the heterogeneous microenvironment around the roots of the aquatic plant *Littorella uniflora*. The presented approach of combining hyperspectral sensing with signal deconvolution is flexible and can easily be adapted for use of various multi-indicator- or even multianalyte-based optical sensors with different spectral characteristics, enabling high-resolution simultaneous imaging of multiple analytes.

KEYWORDS: hyperspectral imaging, planar optodes, chemical imaging, image analysis, chemometrics, linear unmixing

In natural systems including environmental and medical samples, the activity of different metabolic processes leads to changes in analyte dynamics or distributions, which are often coupled relative to each other and the underlying sample structure. Thus, simultaneous monitoring of several analytes at the exact same position is of high interest when working with complex, natural samples.^{1,2} Chemical imaging of analyte dynamics with luminescent optical sensors (so-called optodes) has undergone a rapid development and is now used in a variety of research areas.^{3,4} The main detection methods are (i) intensity-based imaging (Figure 1A) employing an analyte-sensitive indicator dye and an inert reference dye to allow ratiometric read out^{3,5} and (ii) lifetime-based imaging,⁶ which is either done in the time domain^{7,8} or the frequency domain.^{9,10} Lifetime-based imaging techniques are prone to less interferences than intensity-based imaging techni-

ques.^{6,11,12} The equipment, however, is more complex and expensive, and although camera systems are limited to imaging a maximum of two indicator dyes, that is, two analytes, simultaneously,^{13,14} single indicator-based optodes are the standard for this imaging approach. In comparison, ratiometric imaging systems are comparatively cheap^{3,15,16} and can be realized with many different camera systems ranging from simple handheld color cameras to high-end camera solutions. Typically, this provides the user with three to four color

Received: October 5, 2020

Accepted: December 8, 2020

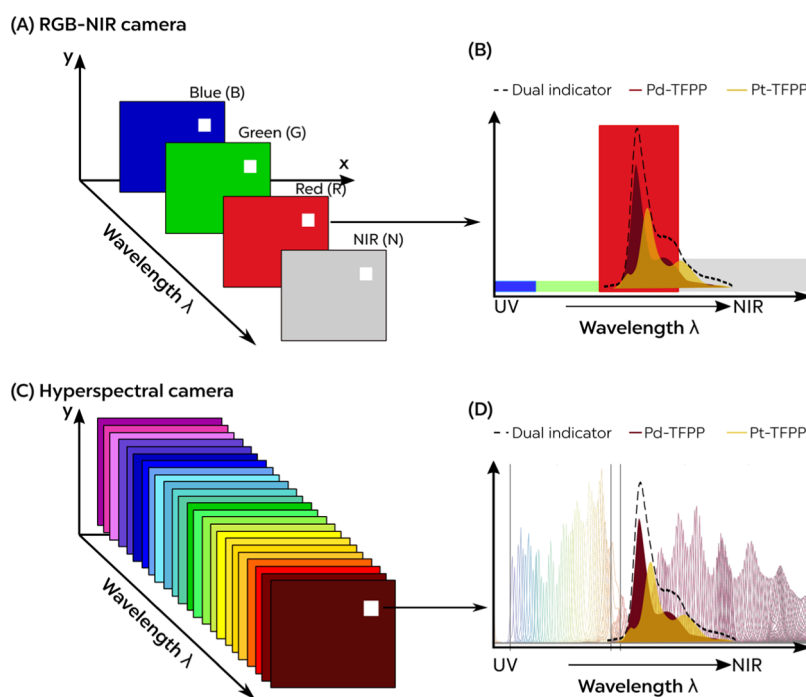


Figure 1. Comparison of (A) a 4-channel RGB-NIR system (e.g., ref 17) with (C) a 150+ band hyperspectral camera system (SnapScan, Imec) and (B, D) respective information obtained for the emission spectrum from individual and combined optical O₂ sensors. As camera systems based on Bayer filters (A) provide discrete signal information in three to four different spectral windows, it is impossible to extract detailed information of individual indicator contributions and only an overall intensity value can be extracted. Hyperspectral camera systems (C) record a full spectrum (in this case over more than 150 spectral bands between ~470 and 900 nm) of the sensor luminescence at high spectral resolution enabling postacquisition deconvolution of the signal into contributions from specific sensor components (D).

channels (red, green, and blue (RGB)³ and RGB + NIR^{15,17}) for sensor readout, typically from a reference dye and two indicator dyes that are excited in the UV–blue spectral region (Figure 1A). However, it is important that the luminescent dyes show minimal spectral overlap with each other, with emission spectra that match the sensitivity of the color channels of the camera system, to minimize crosstalk between the channels. Alternatively, more complex camera systems in combination with filter wheels can be used¹⁸ to provide more working windows for sequential imaging of multiple analytes, but ratiometric approaches are inherently limited by the use of band- or long-pass filters and signal integration over different discrete spectral windows.

A different approach to imaging complex spectral signatures originates from remote sensing,¹⁹ where the use of hyperspectral cameras enables acquisition of image stacks, providing spectral information for each individual pixel. In contrast to imaging with typical color cameras based on a red, green, and blue channel, hyperspectral imaging systems collect spectral information across the visible and near-infrared spectral range in each pixel. Hyperspectral camera systems are frequently used airborne, for example, for large-scale satellite imaging of the Earth's surface,^{19,20} but as camera technology has become more compact and affordable, hyperspectral imaging is increasingly used at smaller scales, for example, on drones, in the food industry for quality control,²¹ in medical diagnostics,¹⁹ or in environmental science.^{22,23} However, despite their tremendous potential for sensor readout, such hyperspectral cameras have not yet been used for chemical imaging of luminescent dyes. Although this might partly be due to the challenge of deconvoluting superimposed spectral signals without loss in sensitivity or specificity of the sensor system,

spectral deconvolution of hyperspectral images is well established in remote sensing and other spectroscopic disciplines. In magnetic resonance spectroscopy for instance, signal deconvolution is used for spectral resolution amelioration²⁴ and in multispectral fluorescence microscopy, it is successfully applied, for example, via linear unmixing or singular value decomposition approaches to determine the percent contribution of different individual fluorophores to the total measured signal in each pixel.^{25–27}

Here, we present the first use of a hyperspectral camera system for chemical imaging in combination with a mathematical approach for signal deconvolution of sensor signals generated by two overlapping luminescence indicators with different dynamic range co-immobilized in a planar optode. We used two sets of well-known O₂ indicators: (i) a red-emitting Pd(II)/Pt(II) tetrakis(pentafluorophenyl)porphyrin-(TFPP) dual-indicator sensor and (ii) a near-infrared (NIR)-emitting Pd(II)/Pt(II) meso-tetraphenyltetra-benzoporphyrin-(TPBTP) dual-indicator sensor, where the Pd(II)-based sensors are typically used as O₂ trace sensors with high sensitivity but a narrow dynamic range.^{28–30} This novel approach enables a more sensitive imaging of dissolved oxygen over the full concentration range between 0–950 hPa, as demonstrated by high-resolution hyperspectral imaging of the O₂ distribution in the heterogeneous microenvironment around the roots of the aquatic plant *Littorella uniflora*. The combination of sensor readout with a fast-scanning hyperspectral imaging camera and a signal deconvolution algorithm enables multi-indicator-based imaging without spectral limitations and can potentially be applied to other dual-indicator sensor systems, paving the way for novel multianalyte imaging approaches.

EXPERIMENTAL SECTION

Camera Setup. Different acquisition methods are employed in hyperspectral cameras.^{31,32} In this study, we used a novel fast-recording line-scan hyperspectral camera system (Imec SnapScan VNIR camera; imec-int.com, Belgium), which records hyperspectral image cubes by moving a special filter plate in front of the camera chip.^{33,34} This enables hyperspectral imaging with up to 150 bands/channels covering a wavelength range from ~470 to 900 nm (Figure 1B) at high spatial resolution (17 μm per pixel; 7Mpx per band). A color-corrected objective (Apo-Xenoplan lens, f2.0; Schneider-Kreuznach GmbH, Germany) was mounted on the camera, which was connected to a PC and controlled using hyperspectral image-recording software (HSI Snapscan v1.4.1.0; imec-int.com, Belgium). For acquisition of a single hyperspectral cube, the camera was set to scan the full image frame [1088 \times 2048 pixels (H \times W)] and full spectral wavelength range (~470–900 nm) with a pixel step of 3 nm and an integration time of 100 ms. The pixel blur and binning were set to 0 and 1, respectively. The overall acquisition time for one hyperspectral image cube using the described settings was 66 s.

Planar sensor foils (see detailed sensor preparation in the Supporting Information) were excited with a high-power LED light source (460 nm; LED Hub, Omicron Laserage Laserprodukte GmbH, Rodgau, Germany) equipped with a 1 m liquid light guide and a collimating lens and controlled via a PC running the manufacturers' software. To avoid optical crosstalk between the LED and camera, a 475 nm short-pass filter (475 nm, OD 4.0; Edmund Optics Inc., edmundoptics.com, USA) was mounted in front of the LED light guide.

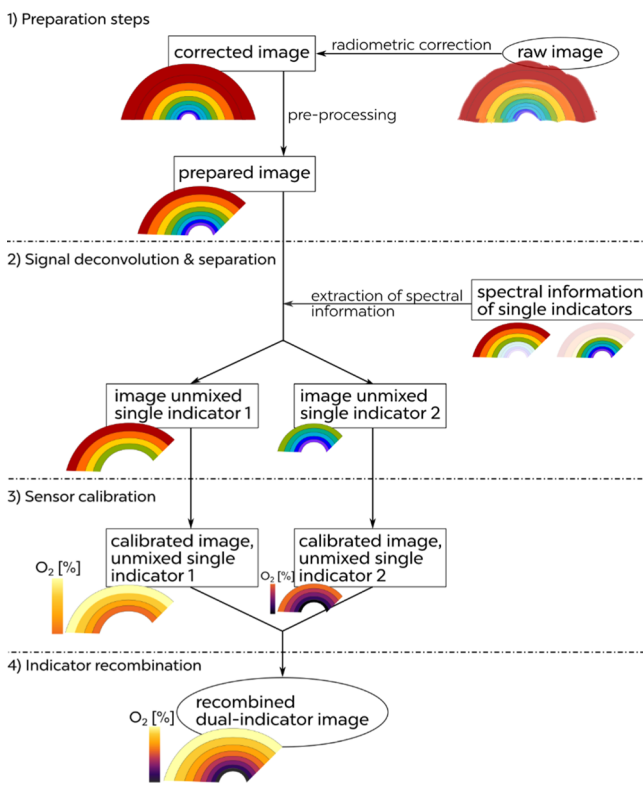
Biological Application. A sandwich chamber for imaging dissolved oxygen dynamics in the rhizosphere of the aquatic plant *L. uniflora* was prepared according to the literature.¹⁰ Briefly, the planar optode containing the O₂-sensitive indicator dyes was fixed on a glass slide using a thin water film and tape. Trapped air bubbles were carefully removed using a soft tissue to avoid scratching of the indicator layer. A second glass slide, with three microscope slides (0.1 cm thickness) glued on three sides as spacers, was filled with sieved sediment (mesh size <0.5 mm), leaving approx. 2 cm free below the open side. The roots of *L. uniflora* were carefully placed on the sediment and the leaves above the sediment were kept moist. The sandwich chamber was carefully closed without entrapping air bubbles. Clamps were used to secure the two glass plates and playdough was used to seal the sides. The sandwich chamber was carefully placed into an aquarium, slightly tilted to facilitate root growth toward the planar optode, and kept under light (148 $\mu\text{mol photons m}^{-2} \text{ s}^{-1}$; 400–700 nm)/dark conditions (13 h/11 h) to allow equilibration prior to measurement. Before each measurement, the external illumination was switched off and images were acquired for both dual-indicator sensors.

Data Processing. Required Programming Packages. The radiometric correction of the raw image stacks (hyperspectral cubes) is done using a MATLAB script that can be obtained from the camera manufacturer upon request (hsisupport@imec.be). The presented algorithms for the single- and dual-indicator calibration and evaluation are self-coded using Python 3.7.4 (python.org). For execution of the code, the following Python packages are required: For loading and processing hyperspectral images, we used Spectral Python (SPy, spectralpython.net), matplotlib (matplotlib.org), and Python Imaging Library (PIL; pypi.org/project/Pillow); for curve fitting and solving the integration and the optimization problem, SciPy (scipy.org) and the nonlinear least-squares fitting (*lmfit*; lmfit.github.io) were used. Further packages required are *numpy*, *pandas*, *math*, *random*, *time*, *glob*, *pathlib*, *os*, *hSpy*, and *xrld*. All libraries required were to date at the time the paper was submitted. The Python code can be downloaded from GitHub (github.com/silviaelisabeth/Signal-deconvolution-in-optical-chemical-imaging-for-reliable-multi-analyte-sensing) and is openly accessible.

Workflow for Image Analysis and Signal Deconvolution. The following procedures for indicator calibration and evaluation are a descriptive summary of the individual mathematical steps carried out.

Scheme 1 provides an overview of the individual process steps, and the Supporting Information provides a more detailed description of the programming code.

Scheme 1. Workflow for Image Analysis and Signal Deconvolution to Enable Broad-Range Sensing of Dissolved O₂ Using Linear Unmixing on Hyperspectral Sensor Data



Preparation Steps. First, acquired image stacks (raw images, also known as hyperspectral cubes) were radiometrically corrected using the angularity model described by Pichette et al.³⁵ A preprocessing step is included for all acquired and radiometrically corrected hyperspectral images in order to remove redundant information to accelerate the analysis of subsequent evaluation steps. The preprocessing of the images includes an extraction of regions of interest (RoIs), in which the spectral information is collected, and the determination of average intensities along the wavelength range within each RoI, among others. Outliers are also removed and replications of the same concentration point are merged by averaging the respective spectra. After these preparation steps, the corrected and prepared images are used for signal deconvolution and separation.

Signal Deconvolution and Separation Using Linear Unmixing. To deconvolute the hyperspectral images and to extract the individual contribution of the single indicators to the superimposed signal, we used a linear unmixing approach described by Hiraoka et al.³⁶ Here, the superimposed sensor signal recorded with the hyperspectral camera is assumed as a linear combination of the signals from the two indicators and the reference dye. Using a generic spectrum of each dye, the superimposed spectrum can be separated to determine the contribution of each dye (linear unmixing). The process of linear unmixing is visualized in Figure 2 and summarized in equation (eq 1)

$$\psi(\lambda, O_2) = \alpha(O_2) \cdot \varphi(\lambda, Pd) + \beta(O_2) \cdot \varphi(\lambda, Pt) \quad (1)$$

where φ is the spectral response of the single indicators and α and β are the O₂-sensitive coefficients (contributions). ψ is the superimposed signal recorded with the hyperspectral camera. The coefficients (α , β) for each single indicator are determined with a sequential least-squares fit (eq S4).

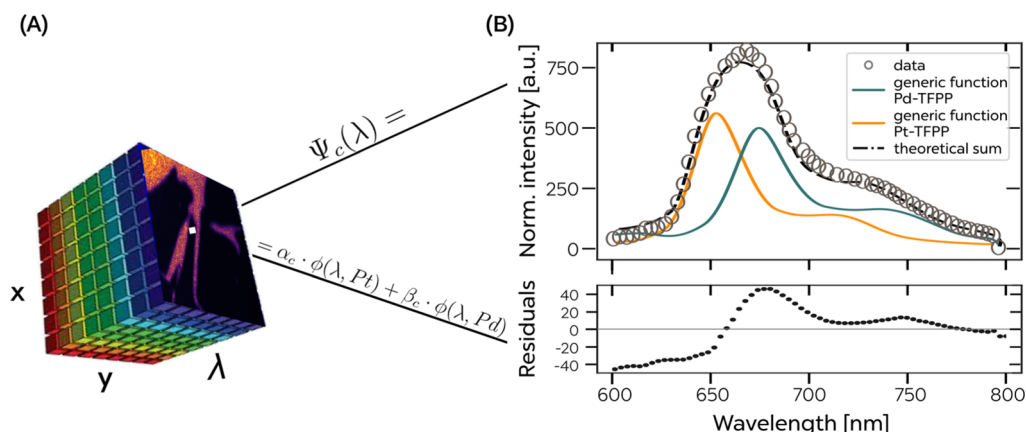


Figure 2. From the hyperspectral cube to signal separation using linear unmixing. The superimposed signal (ψ) is extracted from the radiometrically corrected hyperspectral cube (A). Signal deconvolution is achieved by applying a linear unmixing approach, assuming that the individual indicators [$\varphi(\text{Pt})$ and $\varphi(\text{Pd})$] are not interacting with each other and contribute linearly to the total signal. Panel (B) exemplifies the linear unmixing for a porphyrin-based (Pd–TFPP/Pt–TFPP) dual-indicator under anoxic conditions. The superimposed spectrum (ψ) recorded on the hyperspectral camera is indicated with open symbols (\circ), whereas the individual indicators are indicated as colored solid lines. The hypothetical sum of both individual indicators multiplied with their respective coefficient [α for $\varphi(\text{Pt})$ and β for $\varphi(\text{Pd})$] is shown as a black dashed line coinciding with the superimposed signal. The spectral deviation of the theoretical sum from the actual measured signal is shown in the residuals.

To determine a mathematical function for the spectral response of the single indicators (φ) based on sample data, the hyperspectral images of the respective single indicators are used at the three lowest O_2 concentrations (0–60 hPa), that is, the highest luminescence signal intensities. The prepared images at these calibration points are normalized to the maximal indicator intensity and averaged afterward (Figure S3). A self-coded Python script allows the curve fitting of the sample data, assuming a combination of two Voigt profiles and one Gaussian profile to describe the spectral response: the indicator dye and the reference dye are described with a Voigt profile, while the background noise is fit with a Gaussian profile. The generic function of the spectral response (φ) is then used in a sequential least-squares fit to determine the contribution of each single O_2 indicator to the superimposed signal at each calibration point (eq 1). Figure S4 exemplifies the signal deconvolution and separation of the TPTBP dual-indicator sensor at each calibration point using linear unmixing.

Sensor Calibration. The calibration of all indicators, the unmixed single indicators and the respective single indicators, follows the same protocol. First, the integral of the indicator dye emission and the reference dye emission is determined using Simpson's rule for numerical integration of definite integrals.³⁶ The integration limits used are listed in Table S1. Afterward, the integral of the indicator dye is divided by the integral of the reference dye to obtain the ratio at each calibration point, thus allowing a ratiometric evaluation. The ratio is then fit against the analyte concentration using the simplified two-side Stern–Volmer fit as it is commonly done for O_2 sensors (eq S4).^{37,38}

Indicator Recombination for Dual-Indicator Imaging. Recombination of the unmixed and calibrated single indicators is done to achieve broad-range imaging of dissolved O_2 within one dual-indicator sensor, as both indicators exhibit highest sensitivity in different concentration ranges. The recombination is done with regard to the slopes of the calibration curves of the corresponding indicator pair, as shown in Figure S5. The calibration curves for the respective single indicators were stepwise linearized and the slopes of the linear regression were compared between the indicators to identify the steeper slope. The indicator with the steeper slope is used in the respective concentration range, indicating a higher analyte sensitivity.

RESULTS AND DISCUSSION

The idea of multi-indicator chemical imaging is not new, and several attempts have been proposed in the literature,^{15,39–41} where signal separation and deconvolution of the multiple

indicator signals are generally accomplished by either taking advantage of different lifetimes or different spectral properties of the indicators. Nevertheless, successful multi-indicator imaging with luminescent sensors has been limited to only a few examples,^{17,27,39,42–44} where the used imaging approaches impose high spectral constraints on the choice of indicators, hindering full deconvolution of overlapping luminescence signals. We developed a novel hyperspectral approach for optical chemical imaging with multiple sensor dyes that have overlapping spectral emission characteristics. We (i) describe a hyperspectral measuring setup for O_2 imaging with planar optodes over a wide dynamic range, (ii) describe a novel data analysis approach for signal deconvolution of two overlapping luminescent indicators, and (iii) demonstrate its applicability for multi-indicator imaging without spectral limitations. In the following, we first describe and discuss the hyperspectral image acquisition approach and the subsequent image analysis including signal deconvolution. Then, we demonstrate an application of the novel chemical imaging approach for mapping O_2 distributions in sediments surrounding the roots of an aquatic plant.

Camera Characteristics. The use of a hyperspectral camera abolishes spectral restrictions compared to that of multichannel color cameras or monochrome cameras in combination with filter wheels. In our study, we used a camera system providing >150 spectral bands between ~470 and 900 nm with a spectral resolution of up to <1–10 nm and a very good pixel resolution of 17 μm . A shortcoming of this specific hyperspectral camera when imaging luminescence signals is the need for a radiometric correction of each hyperspectral image stack that needs to be conducted after each acquisition. The corresponding script and all Supporting Information for correction can be obtained from the manufacturer upon request; however, it has to be noted that the correction procedure is under development and still requires improvements, as some spectral artifacts remain, notably in the wavelength range between 600 and 650 nm, where the different zones of the spectral filters overlap and change.⁴⁵ This results in a noisy and slightly distorted signal in

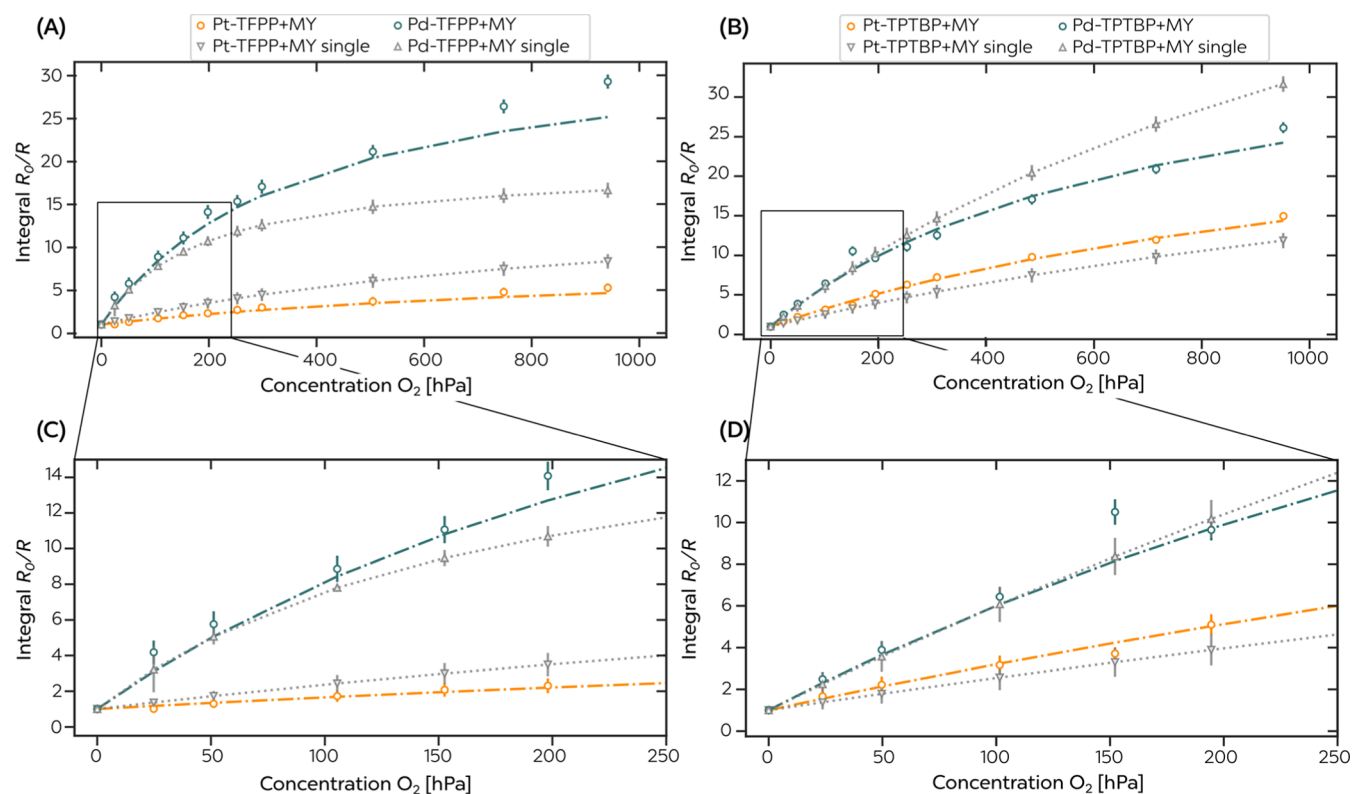


Figure 3. Calibration curve of the dual-indicator O_2 sensors compared to that of the corresponding single-indicator O_2 sensors. (A) Calibration curves of the unmixed dual-indicator Pt–TFPP/Pd–TFPP O_2 optode and (B) calibration curves of the unmixed dual-indicator Pt–TPTBP/Pd–TPTBP O_2 optode over the full calibration range between 0 and 950 hPa. The coefficients of the unmixed dual indicators are determined by linear unmixing and are marked in colors for each indicator. The corresponding fit for the associated single indicator is shown in gray colors and dotted lines. Error bars indicate the standard deviation of the respective indicator. Panels (A,B) show the whole calibration range from 0 to 950 hPa and panels (C,D) are zoom-ins between 0 to 200 hPa.

that specific wavelength range, thus affecting the performance of the signal deconvolution algorithm. Even though the artifacts are addressed by fitting the corresponding region with a noise function assuming a Gaussian profile, the instrumental noise becomes prevalent at higher O_2 concentrations and low indicator signals (Figure S4). However, there are many different hyperspectral camera systems on the market and our approach of combining hyperspectral sensor readout with signal deconvolution is not linked to a particular hyperspectral camera.

Workflow for Image Analysis and Signal Deconvolution. *Signal Deconvolution and Separation Using Linear Unmixing.* An overview of the principle of the signal deconvolution is shown in Figure 2, and the performance of the linear unmixing algorithm is exemplified for the TPTBP dual-indicator O_2 sensor in Figure S4. The algorithm performs well, assuming a linear contribution of all indicators without any cross-interaction because of the spectral overlap of the respective absorption and/or emission spectra. The theoretical sum of the contributing indicators coincides with the measured superimposed signal, resulting in only minor spectral deviations.

However, at high O_2 concentrations, that is, low luminescence signal intensities, the performance of the linear unmixing decreased slightly as the deviation of the hypothetical sum of the two indicators from the superimposed signal increased (Figure S4). One reason for this might be that the algorithm always assumes a contribution of both indicators to

the superimposed signal and thus overestimates the contribution of the Pd-based indicator at high O_2 concentrations.

The generic, mathematical description of the spectral response of the single indicators φ was done by curve fitting of sample data at the highest signal intensity to reduce the influence of artifacts. As the spectral descriptions of the indicators are crucial for the performance of the signal deconvolution, the curve fits were validated with a state-of-the-art spectrometer. The results are shown in Figure S2. In all cases, the spectral deviation was low as indicated by the small residuals (≤ 0.3 for TFPP indicators and ≤ 0.2 for TPTBP indicators).

Sensor Calibration and Limit of Detection. For the calibration of the single- and dual-indicator O_2 sensors, we used an integral-based approach instead of the standard approach using the maximal intensity. Although the intensity approach is the standard approach using certain wavelengths indicating the maximal emission intensity of the indicator and reference dye,⁴⁴ the integral approach determines the integral under the emission curve of the indicator and the reference using Simpson's rule for numerical integration of definite integrals.³⁶ Both approaches are equally valid; however, because the evaluation of the dual-indicator sensor is based on the integration of the generic functions of the single indicators, we decided to use the integral approach for the single indicators as well.

In Figure 3, calibration curves for the single and unmixed dual indicators are compared. In terms of their signal ratio R_0/R , the unmixed dual indicators exhibit a distorted calibration

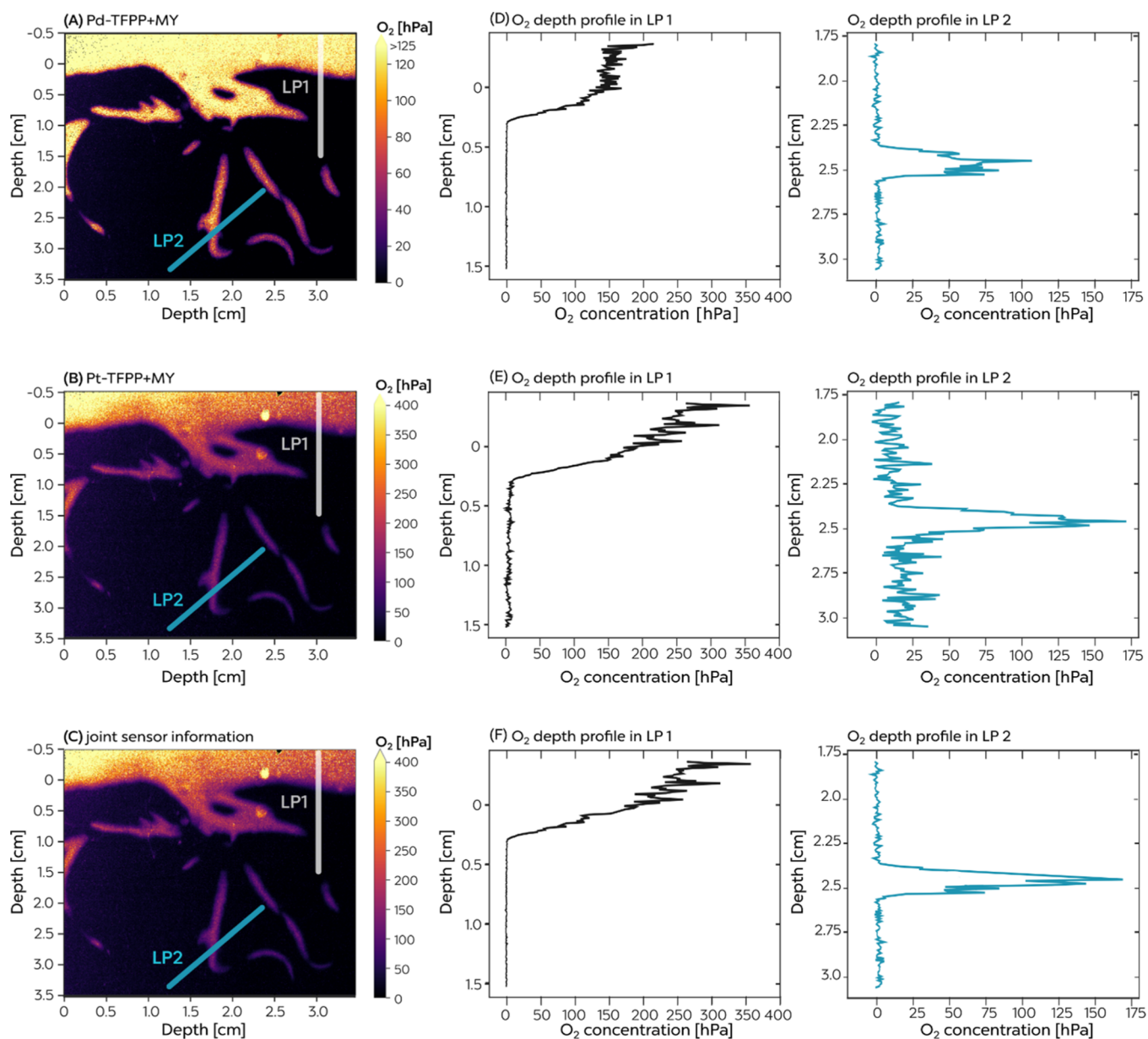


Figure 4. Mapping of O₂ in sediment around the roots of the freshwater plant *L. uniflora* in light using the TFPP dual-indicator sensor (Pd–TFPP/Pt–TFPP) in combination with a hyperspectral camera system. Panels (A–C) visualize the dissolved O₂ concentration in each pixel of the image frame, as calculated using a linear unmixing approach. Panels (A,B) show results from the individual indicators upon signal separation, whereas panel (C) combines the results of both indicators, enabling high-resolution broad-range imaging. The corresponding panels (D–F) are examples of O₂ concentration profiles extracted from the O₂ images along two line profiles (LPs), as marked as colored (LP1 = white, LP2 = blue) straight lines in the image frame.

curve compared to the corresponding single indicator, especially at higher O₂ concentrations. This distortion results in an amended sensitivity and limit of detection (LoD). The amended sensitivity can also be described by the calibration parameters of the simplified Stern–Volmer fit (cf. Table S2), notably in the quenching constant K_{sv} and the ratio of the quenching constants for the respective indicator analogues (Pd–/Pt–TFPP or Pd–/Pt–TPTBP). For the TFPP dual-indicator sensor, the ratio of the quenching constants is greatly overestimated compared to the corresponding ratio of the single indicators (11.38 vs 6.69 for the dual-indicator and single-indicator sensors, respectively). The LoD of the dual indicator (0.03 hPa), as calculated from eq S1, is reduced compared to that of the single indicators (0.15 hPa and 2.87

hPa for Pd–TFPP and Pt–TFPP, respectively). For the TPTBP system, however, both parameters, that is, the LoD and the K_{sv} ratio, are diminished compared to the corresponding parameters of the single indicator. The LoD of the dual-indicator sensor is intermediate (1.00 hPa) compared to the LoD of the single indicators (0.73 hPa and 1.63 hPa for Pd–TPTBP and Pt–TPTBP, respectively) and the K_{sv} ratio changes from 2.0 to 3.18. As mentioned above, one reason for the over- or underestimation of the unmixed dual-indicator sensors is that the performance of the signal deconvolution decreases at higher O₂ concentrations, where the instrument noise becomes prevalent while the algorithm tries to include both indicators in the linear combination (Figure S4). However, as these factors are either instrumental-

based or result from the algorithm, the bias is reproducible and is addressed by the calibration. The rather high indicator concentration for the dual-indicator sensor may lead to aggregation, thus affecting the sensor sensitivity as well. However, preliminary tests showed no sign of aggregation, which is why we aimed to get sufficient signals at a reasonable exposure time, which allowed for imaging the chemical microenvironment at high temporal resolution.

Indicator Recombination for Dual-Indicator Imaging. Because both indicators image the same analyte but exhibit different sensitivities over different concentration ranges, the results of the unmixed indicators must be recombined to a joint result of the dual-indicator sensor. The recombination was done with regard to the slopes of the (partially) linearized calibration curves of the corresponding indicator pair, as shown in Figure S5. A steeper slope correlated with higher analyte sensitivity, resulting in a more accurate analyte sensing. For the porphyrin-based dual-indicator sensor (Pd–/Pt–TFPP), the Pd-analogue exhibited a steeper slope of the calibration curve as compared to the Pt-analogue in the O₂ concentration range between 0 and 125 hPa, meaning that Pd–TFPP dominated the dual-indicator O₂ sensor within this concentration range, while Pt–TFPP dominated the dual-indicator sensor at higher O₂ concentrations. The benzoporphyrin-based dual-indicator O₂ sensor (Pd–/Pt–TPTBP) was dominated by the Pd-analogue until 355 hPa, as the Pd-analogue showed a steeper slope in the lower O₂ concentration range. At higher O₂ concentrations, the Pt-analogue predominated the response of the dual-indicator sensor. By combining the readout of the dual-indicator O₂ optode with subsequent signal analysis, it thus becomes possible to realize a better sensor response over a wider dynamic range.

Application of the Dual-Indicator Sensor for Imaging O₂ as a Trace and Broad-Range Sensor in High Resolution. We tested the applicability of the dual-indicator sensors on a real-life sample, by mapping the dissolved O₂ concentration in the rhizosphere of the freshwater plant *L. uniflora* via hyperspectral luminescence imaging. During cultivation, the plant was kept under experimental light/dark conditions (13 h/11 h). Prior to measurement, the plant was illuminated for 30 min under a photon irradiance (400–700 nm) of 148 $\mu\text{mol photons m}^{-2} \text{s}^{-1}$. Photosynthesis of the plant and translocation of produced O₂ to its roots led to oxygenation of the rhizosphere sediment. Here, we discuss the results of the TFPP dual-indicator sensor (Figure 4), while the corresponding results for the TPTBP dual-indicator sensor are presented in the Supporting Information (Figure S6).

Images of the O₂ distribution around the plant root as determined with the unmixed TFPP dual-indicator O₂ sensors are shown in Figure 4A,B. The O₂ concentration was determined in each pixel for the unmixed indicators and recombined to a broad-range dual-indicator sensor, as shown in Figure 4C. To analyze the O₂ dynamics in more detail, two different line profiles (LPs) were selected in the images. The first LP shows a depth profile (LP1) of the soil–water interphase and the second LP (LP2) is a cross-section of the microenvironment around the root of the plant. Depth-resolved O₂ concentration gradients are shown in Figure 4D–F. Figure 4F shows the broad-range dual-indicator O₂ sensor readout as a recombination of the unmixed indicators shown in Figure 4D,E. Although the Pd-analogue O₂ sensor readout exhibited high sensitivity at low–moderate O₂ levels, its readout at higher O₂ levels became noisier and even

approached an upper limit significantly underestimating the “true” O₂ concentration (Figure 4A). In comparison, the Pt-analogue sensor exhibited a more noisy signal at low O₂ levels with a small offset of the zero levels, while it showed a much better signal quality at high O₂ concentrations (>125 hPa). By combining the benefits of both indicators, the Pd-indicator for trace O₂ and the Pt-indicator for higher O₂ concentrations, the new broad-range dual-indicator sensor allowed sensitive imaging of dissolved O₂ over the full concentration range between 0 and 950 hPa (Figure 4F).

CONCLUSIONS

We have developed a novel approach for using multi-indicator optodes in combination with hyperspectral luminescence imaging and signal deconvolution of overlapping emission spectra. The signal analysis algorithm is based on well-established principles for signal separation and deconvolution in spectroscopy and multispectral fluorescence microscopy. It assumes that the superimposed luminescence spectrum from a multi-indicator optode can be described as a linear combination of individual spectra without any indicator interactions. Sequential least-squares fitting then determines the contribution of the individual indicators to the combined sensor signal. We demonstrated the novel approach using a fast-scanning hyperspectral camera system in combination with an optode containing two luminescent O₂ indicators, allowing broad-range imaging of dissolved O₂. Although linear unmixing leads to some distortion of the calibration curve for the unmixed indicators because of reduced deconvolution performance at higher O₂ concentrations (lower signal intensities), the recombination of the respective unmixed indicators to a joint, broad-range dual-indicator O₂ sensor enables sensitive imaging of O₂ dynamics over the full concentration range between 0 and 950 hPa with less-noisy results. The applicability of the method and the dual-indicator O₂ planar optodes was demonstrated by imaging the O₂ microenvironment around the roots of the aquatic plant *L. uniflora*. The combination of hyperspectral imaging and signal deconvolution enables multi-indicator imaging without spectral limitations and can easily be applied to other dual-indicator sensor systems. Hyperspectral luminescence imaging in combination with signal deconvolution can thus overcome the spectral restrictions of current optode readout systems and now enables multi-indicator chemical imaging at high spatial and temporal resolution. This approach tailors a new generation of optical chemical multianalyte sensors for diverse applications such as monitoring complex dynamics of covarying environmental parameters in natural samples.

ASSOCIATED CONTENT

Supporting Information

The Supporting Information is available free of charge at <https://pubs.acs.org/doi/10.1021/acssensors.0c02084>.

Measurement setup for imaging planar O₂ optodes, workflow of the linear unmixing, full spectrum recorded on the hyperspectral camera, and recombination of the unmixed dual indicators for joint imaging (PDF)

AUTHOR INFORMATION

Corresponding Authors

Silvia E. Zieger – Aarhus University Centre for Water Technology (WATEC), Department of Biology, Section for

Microbiology, Aarhus University, 8000 Aarhus C, Denmark;
 orcid.org/0000-0002-1952-6294; Email: szieger@bio.au.dk

Klaus Koren – Aarhus University Centre for Water Technology (WATEC), Department of Biology, Section for Microbiology, Aarhus University, 8000 Aarhus C, Denmark; Email: klaus.koren@bio.au.dk

Authors

Maria Mosshammer – Marine Biological Section, Department of Biology, University of Copenhagen, 3000 Helsingør, Denmark

Michael Kühl – Marine Biological Section, Department of Biology, University of Copenhagen, 3000 Helsingør, Denmark

Complete contact information is available at:

<https://pubs.acs.org/10.1021/acssensors.0c02084>

Author Contributions

K.K. and M.K. conceived the project. S.E.Z. and K.K. designed the experiments with support from M.M. and M.K. S.E.Z. performed the experiments and developed the evaluation algorithm. S.E.Z. and M.M. wrote the manuscript with editorial help from K.K. and M.K.

Notes

The authors declare no competing financial interest.

ACKNOWLEDGMENTS

We thank Ronny M. Baaske, Mette L.G. Nikolajsen, and Lars B. Pedersen (Department of Biology, Aarhus University) for excellent technical assistance and Vincent Scholz for his help with the initial preparation of the soil sandwich. We acknowledge the professional assistance in programming provided by Fatemeh Zardbani, Prof. Panagiotis Karras (Department of Computer Science, Aarhus University), and Dr. Lennard Krause (Department of Chemistry, Aarhus University). The study was supported by a research grant from the Grundfos Foundation (K.K.), a Sapere Aude grant (DFF-8048-00057B; K.K.) and a project grant (DFF-8022-00301B; M.K.) from the Independent Research Fund Denmark, and a project grant from the Villum Foundation (00023073; M.K.).

ABBREVIATIONS

SLR camera, single-lens reflex camera; RoI, region of interest; LP, line profile

REFERENCES

- (1) Kühl, M.; Trampe, E.; Mosshammer, M.; Johnson, M.; Larkum, A. W.; Frigaard, N.-U.; Koren, K. Substantial Near-Infrared Radiation-Driven Photosynthesis of Chlorophyll f-Containing Cyanobacteria in a Natural Habitat. *Elife* **2020**, 9. <https://doi.org/10.7554/eLife.50871>.
- (2) Brodersen, K. E.; Koren, K.; Moßhammer, M.; Ralph, P. J.; Kühl, M.; Santner, J. Seagrass-Mediated Phosphorus and Iron Solubilization in Tropical Sediments. *Environ. Sci. Technol.* **2017**, 51, 14155–14163.
- (3) Larsen, M.; Borisov, S. M.; Grunwald, B.; Klimant, I.; Glud, R. N. A Simple and Inexpensive High Resolution Color Ratiometric Planar Optode Imaging Approach: Application to Oxygen and PH Sensing. *Limnol. Oceanogr. Methods* **2011**, 9, 348–360.
- (4) Meier, R. J.; Fischer, L. H.; Wolfbeis, O. S.; Schäferling, M. Referenced Luminescent Sensing and Imaging with Digital Color Cameras: A Comparative Study. *Sens. Actuators, B* **2013**, 177, 500–506.

- (5) Koren, K.; Kühl, M. A Simple Laminated Paper-Based Sensor for Temperature Sensing and Imaging. *Sens. Actuators, B* **2015**, 210, 124–128.
- (6) Koren, K.; Moßhammer, M.; Scholz, V. V.; Borisov, S. M.; Holst, G.; Kühl, M. Luminescence Lifetime Imaging of Chemical Sensors - A Comparison between Time-Domain and Frequency-Domain Based Camera Systems. *Anal. Chem.* **2019**, 91, 3233–3238.
- (7) Holst, G.; Kohls, O.; Klimant, I.; König, B.; Kühl, M.; Richter, T. A Modular Luminescence Lifetime Imaging System for Mapping Oxygen Distribution in Biological Samples. *Sens. Actuators, B* **1998**, 51, 163–170.
- (8) Glud, R.; Ramsing, N.; Gundersen, J.; Klimant, I. Planar Optodes: A New Tool for Fine Scale Measurements of Two-Dimensional O₂ Distribution in Benthic Communities. *Mar. Ecol. Prog. Ser.* **1996**, 140, 217–226.
- (9) Franke, R.; Holst, G. A. Frequency-Domain Fluorescence Lifetime Imaging System (Pco.Flim) Based on a in-Pixel Dual Tap Control CMOS Image Sensor. In *Imaging, Manipulation, and Analysis of Biomolecules, Cells, and Tissues XIII*; Farkas, D. L., Nicolau, D. V., Leif, R. C., Eds.; SPIE BiOS: San Francisco, 2015; Vol. 9328, p 93281K.
- (10) Moßhammer, M.; Scholz, V. V.; Holst, G.; Kühl, M.; Koren, K. Luminescence Lifetime Imaging of O₂ with a Frequency-Domain-Based Camera System. *J. Visualized Exp.* **2019**, 2019, 1–10.
- (11) Santner, J.; Larsen, M.; Kreuzeder, A.; Glud, R. N. Two Decades of Chemical Imaging of Solutes in Sediments and Soils - a Review. *Analytica Chimica Acta*; Elsevier B.V., 2015; pp 9–42.
- (12) Moßhammer, M.; Brodersen, K. E.; Kühl, M.; Koren, K. Nanoparticle- and Microparticle-Based Luminescence Imaging of Chemical Species and Temperature in Aquatic Systems: A Review. *Microchim. Acta* **2019**, 186, 126.
- (13) Nagl, S.; Stich, M. I. J.; Schäferling, M.; Wolfbeis, O. S. Method for Simultaneous Luminescence Sensing of Two Species Using Optical Probes of Different Decay Time, and Its Application to an Enzymatic Reaction at Varying Temperature. *Anal. Bioanal. Chem.* **2009**, 393, 1199–1207.
- (14) Fischer, L. H.; Borisov, S. M.; Schaeferling, M.; Klimant, I.; Wolfbeis, O. S. Dual Sensing of PO₂ and Temperature Using a Water-Based and Sprayable Fluorescent Paint. *Analyst* **2010**, 135, 1224.
- (15) Ehgartner, J.; Wilsche, H.; Borisov, S. M.; Mayr, T. Low Cost Referenced Luminescent Imaging of Oxygen and PH with a 2-CCD Colour near Infrared Camera. *Analyst* **2014**, 139, 4924.
- (16) Ungerböck, B.; Charwat, V.; Ertl, P.; Mayr, T. Microfluidic Oxygen Imaging Using Integrated Optical Sensor Layers and a Color Camera. *Lab Chip* **2013**, 13, 1593–1601.
- (17) Moßhammer, M.; Strobl, M.; Kühl, M.; Klimant, I.; Borisov, S. M.; Koren, K. Design and Application of an Optical Sensor for Simultaneous Imaging of PH and Dissolved O₂ with Low Cross-Talk. *ACS Sens.* **2016**, 1, 681–687.
- (18) Kühl, M.; Behrendt, L.; Trampe, E.; Qvortrup, K.; Schreiber, U.; Borisov, S. M.; Klimant, I.; Larkum, A. W. D. Microenvironmental Ecology of the Chlorophyll B-Containing Symbiotic Cyanobacterium Prochloron in the Didemnid Ascidian Lissoclinum Patella. *Front. Microbiol.* **2012**, 3, 1–18.
- (19) Khan, M. J.; Khan, H. S.; Yousaf, A.; Khurshid, K.; Abbas, A. Modern Trends in Hyperspectral Image Analysis: A Review. *IEEE Access* **2018**, 6, 14118–14129.
- (20) Stuart, M. B.; McGonigle, A. J. S.; Willmott, J. R. Hyperspectral Imaging in Environmental Monitoring: A Review of Recent Developments and Technological Advances in Compact Field Deployable Systems. *Sensors* **2019**, 19, 3071.
- (21) Feng, Y.-Z.; Sun, D.-W. Application of Hyperspectral Imaging in Food Safety Inspection and Control: A Review. *Crit. Rev. Food Sci. Nutr.* **2012**, 52, 1039–1058.
- (22) Kühl, M.; Polerecky, L. Functional and Structural Imaging of Phototrophic Microbial Communities and Symbioses. *Aquat. Microb. Ecol.* **2008**, 53, 99–118.
- (23) Trampe, E.; Kühl, M. Chlorophyll f Distribution and Dynamics in Cyanobacterial Beachrock Biofilms. *J. Phycol.* **2016**, 52, 990–996.

- (24) Paddock, S. W. *Confocal Microscopy, Methods and Protocols*, 2nd ed.; Springer Science & Business Media, 2014.
- (25) Lansford, R.; Bearman, G.; Fraser, S. E. Resolution of Multiple Green Fluorescent Protein Color Variants and Dyes Using Two-Photon Microscopy and Imaging Spectroscopy. *J. Biomed. Optic.* **2001**, *6*, 311.
- (26) Hiraoka, Y.; Shimi, T.; Haraguchi, T. Multispectral Imaging Fluorescence Microscopy for Living Cells. *Cell Struct. Funct.* **2002**, *27*, 367–374.
- (27) Tsurui, H.; Nishimura, H.; Hattori, S.; Hirose, S.; Okumura, K.; Shirai, T. Seven-Color Fluorescence Imaging of Tissue Samples Based on Fourier Spectroscopy and Singular Value Decomposition. *J. Histochem. Cytochem.* **2000**, *48*, 653–662.
- (28) Borisov, S. M.; Gatterer, K.; Klimant, I. Red Light-Excitable Dual Lifetime Referenced Optical PH Sensors with Intrinsic Temperature Compensation. *Analyst* **2010**, *135*, 1711.
- (29) Zach, P. W.; Freunberger, S. A.; Klimant, I.; Borisov, S. M. Electron-Deficient Near-Infrared Pt(II) and Pd(II) Benzoporphyrins with Dual Phosphorescence and Unusually Efficient Thermally Activated Delayed Fluorescence: First Demonstration of Simultaneous Oxygen and Temperature Sensing with a Single Emitter. *ACS Appl. Mater. Interfaces* **2017**, *9*, 38008–38023.
- (30) Quaranta, M.; Borisov, S. M.; Klimant, I. Indicators for Optical Oxygen Sensors. *Bioanal. Rev.* **2012**, *4*, 115–157.
- (31) ElMasry, G.; Sun, D.-W. Principles of Hyperspectral Imaging Technology. *Hyperspectral Imaging for Food Quality Analysis and Control*; Academic Press, 2010; pp 3–43.
- (32) Song, Y. Spatial Resolution Improvement of Hyperspectral Images by Deconvolution and Joint Unmixing-Deconvolution. PhD Thesis, Université de Lorraine, 2019.
- (33) Geelen, B.; Tack, N.; Lambrechts, A. A Snapshot Multispectral Imager with Integrated Tiled Filters and Optical Duplication. *Advanced Fabrication Technologies for Micro/Nano Optics and Photonics VI*, 2013; Vol. 8613, p 861314.
- (34) Tack, N.; Lambrechts, A.; Soussan, P.; Haspeslagh, L. A Compact, High-Speed, and Low-Cost Hyperspectral Imager. *Silicon Photonics VII*, 2012; Vol. 8266, p 82660Q.
- (35) Pichette, J.; Goossens, T.; Vunckx, K.; Lambrechts, A. Hyperspectral Calibration Method For CMOS-Based Hyperspectral Sensors. In *Photonic Instrumentation Engineering IV*; Soskind, Y. G., Olson, C., Eds.; SPIE, 2017; Vol. 10110, p 101100H.
- (36) Horwitz, A. A Version of Simpson's Rule for Multiple Integrals. *J. Comput. Appl. Math.* **2001**, *134*, 1–11.
- (37) Carraway, E. R.; Demas, J. N.; DeGraff, B. A.; Bacon, J. R. Photophysics and Photochemistry of Oxygen Sensors Based on Luminescent Transition-Metal Complexes. *Anal. Chem.* **1991**, *63*, 337–342.
- (38) Borisov, S. M.; Seifner, R.; Klimant, I. A Novel Planar Optical Sensor for Simultaneous Monitoring of Oxygen, Carbon Dioxide, PH and Temperature. *Anal. Bioanal. Chem.* **2011**, *400*, 2463–2474.
- (39) Stich, M. I. J.; Fischer, L. H.; Wolfbeis, O. S. Multiple Fluorescent Chemical Sensing and Imaging. *Chem. Soc. Rev.* **2010**, *39*, 3102.
- (40) Nagl, S.; Wolfbeis, O. S. Optical Multiple Chemical Sensing: Status and Current Challenges. *Analyst* **2007**, *132*, 507.
- (41) Borisov, S. M.; Neurauter, G.; Schroeder, C.; Klimant, I.; Wolfbeis, O. S. Modified Dual Lifetime Referencing Method for Simultaneous Optical Determination and Sensing of Two Analytes. *Appl. Spectrosc.* **2006**, *60*, 1167–1173.
- (42) Schroeder, C. R.; Neurauter, G.; Klimant, I. Luminescent Dual Sensor for Time-Resolved Imaging of PCO₂ and PO₂ in Aquatic Systems. *Microchim. Acta* **2007**, *158*, 205–218.
- (43) Liebsch, G.; Klimant, I.; Frank, B.; Holst, G.; Wolfbeis, O. S. Luminescence Lifetime Imaging of Oxygen, PH, and Carbon Dioxide Distribution Using Optical Sensors. *Appl. Spectrosc.* **2000**, *54*, 548–559.
- (44) Wang, C.; Otto, S.; Dorn, M.; Heinze, K.; Resch-Genger, U. Luminescent TOP Nanosensors for Simultaneously Measuring Temperature, Oxygen, and PH at a Single Excitation Wavelength. *Anal. Chem.* **2019**, *91*, 2337–2344.
- (45) Hagen, N.; Kudenov, M. W. Review of Snapshot Spectral Imaging Technologies. *Opt. Eng.* **2013**, *52* (), 090901. [https://doi.org/ DOI: 10.1117/1.oe.52.9.090901](https://doi.org/10.1117/1.oe.52.9.090901).